

Electronic Supplementary Information

Giant spin-phonon bottleneck effects in evaporable vanadyl-based molecules with long spin coherence

L. Tesi,^a A. Lunghi,^{a,b} M. Atzori,^a E. Lucaccini,^a L. Sorace,^a F. Totti,^a and R. Sessoli^{a,*}

^a Dipartimento di Chimica “Ugo Schiff” e INSTM, Università degli Studi di Firenze, Via della Lastruccia 3, I50019 Sesto Fiorentino (Firenze), Italy

^b School of Physics, CRANN and AMBER Trinity College Dublin 2, Ireland

1. Powder X-ray Diffraction Analysis	2
2. Electron paramagnetic resonance (EPR) spectroscopy	3
3. X-Ray Microtomography	5
4. AC Susceptometry and Magnetometry	5
5. Force Field Calculations Validation	9
References	13

* Correspondence: roberta.sessoli@unifi.it

1. Powder X-ray Diffraction Analysis

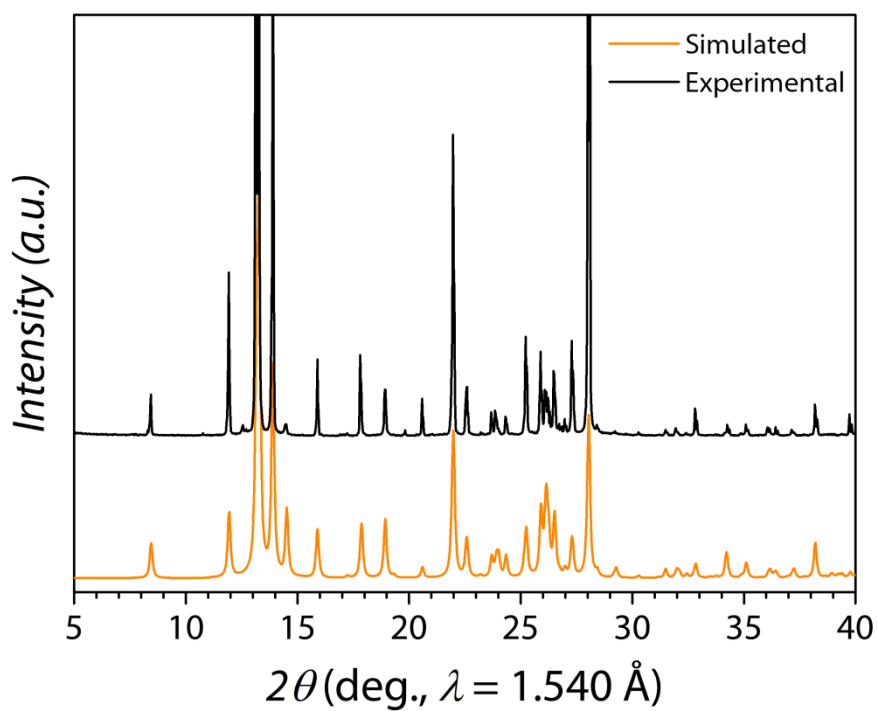


Figure S1. Comparison between experimental (black) and simulated (orange) PXR D patterns ($5\text{--}40^\circ$, 2θ) for **1**.

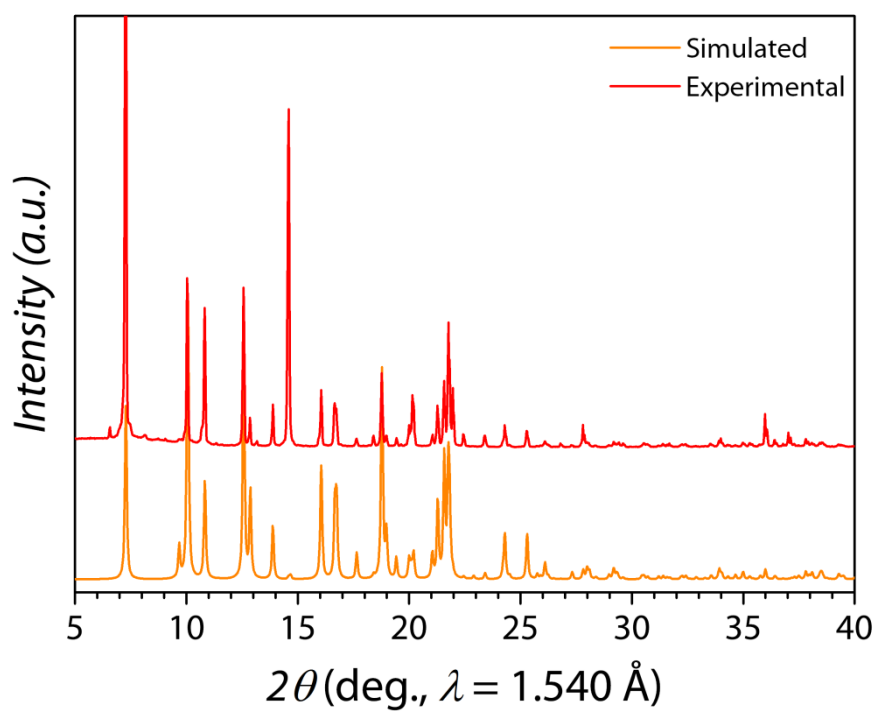


Figure S2. Comparison between experimental (red) and simulated (orange) PXR D patterns ($5\text{--}40^\circ$, 2θ) for **2**.

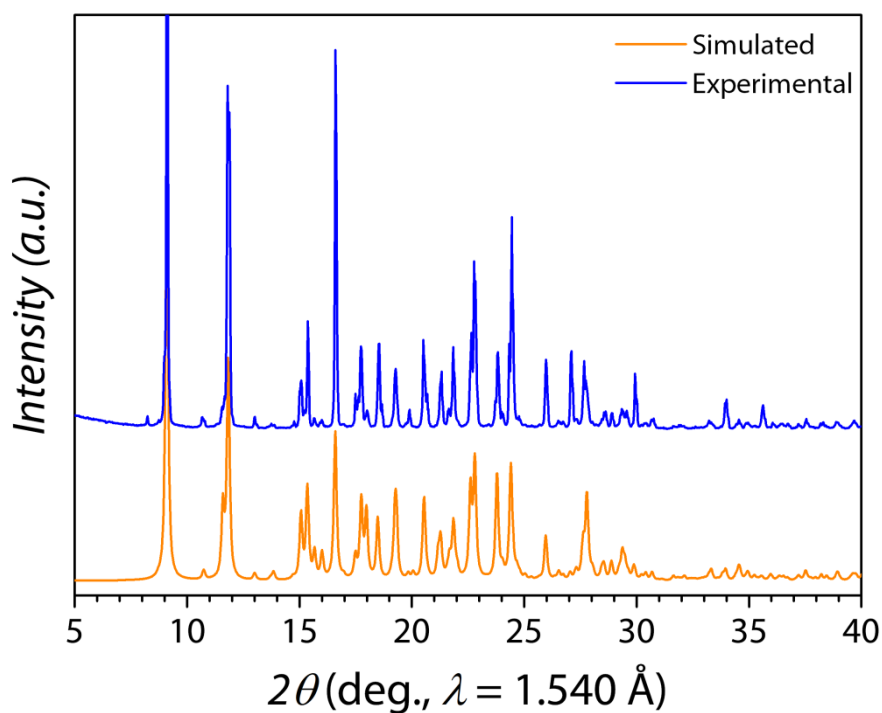


Figure S3. Comparison between experimental (blue) and simulated (orange) PXRD patterns (5–40°, 2θ) for **3**.

2. Electron paramagnetic resonance (EPR) spectroscopy

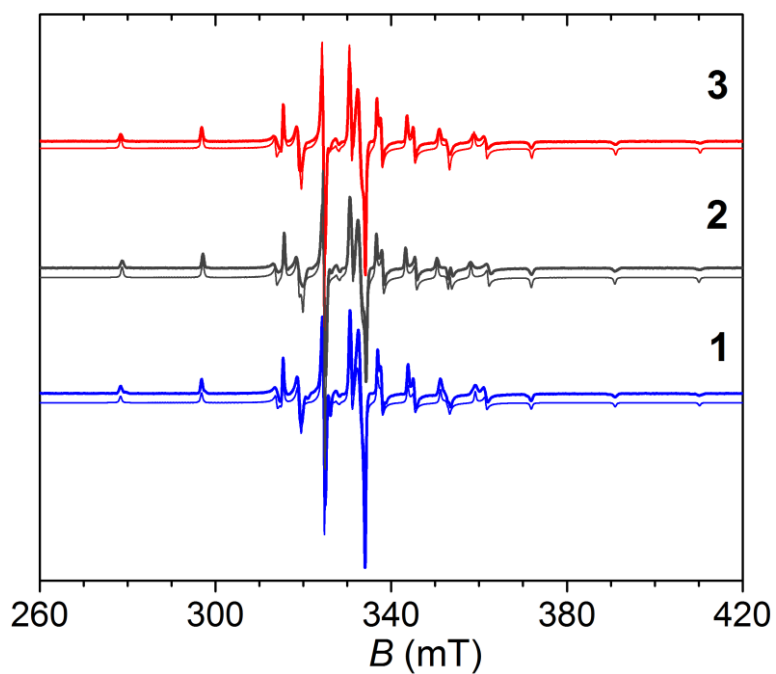


Figure S4. X-band spectra of frozen solutions (1 mM, 2:3 toluene: CH_2Cl_2) of **3**, **2** and **1** (thick lines) recorded at $T= 50$ K and best simulated spectra (thin lines) obtained with parameters reported in Table S1.

Table S1. Best simulation Spin Hamiltonian parameters of X-band EPR spectra of **1**, **2** and **3** assuming collinearity of g and A tensors.

	1	2	3
g_x	1.9845	1.9855	1.9845
g_y	1.981	1.980	1.981
g_z	1.9477	1.947	1.9466
A_x (cm ⁻¹)	0.0058	0.0056	0.00575
A_x (cm ⁻¹)	0.00627	0.00635	0.0063
A_z (cm ⁻¹)	0.01712	0.01705	0.01712

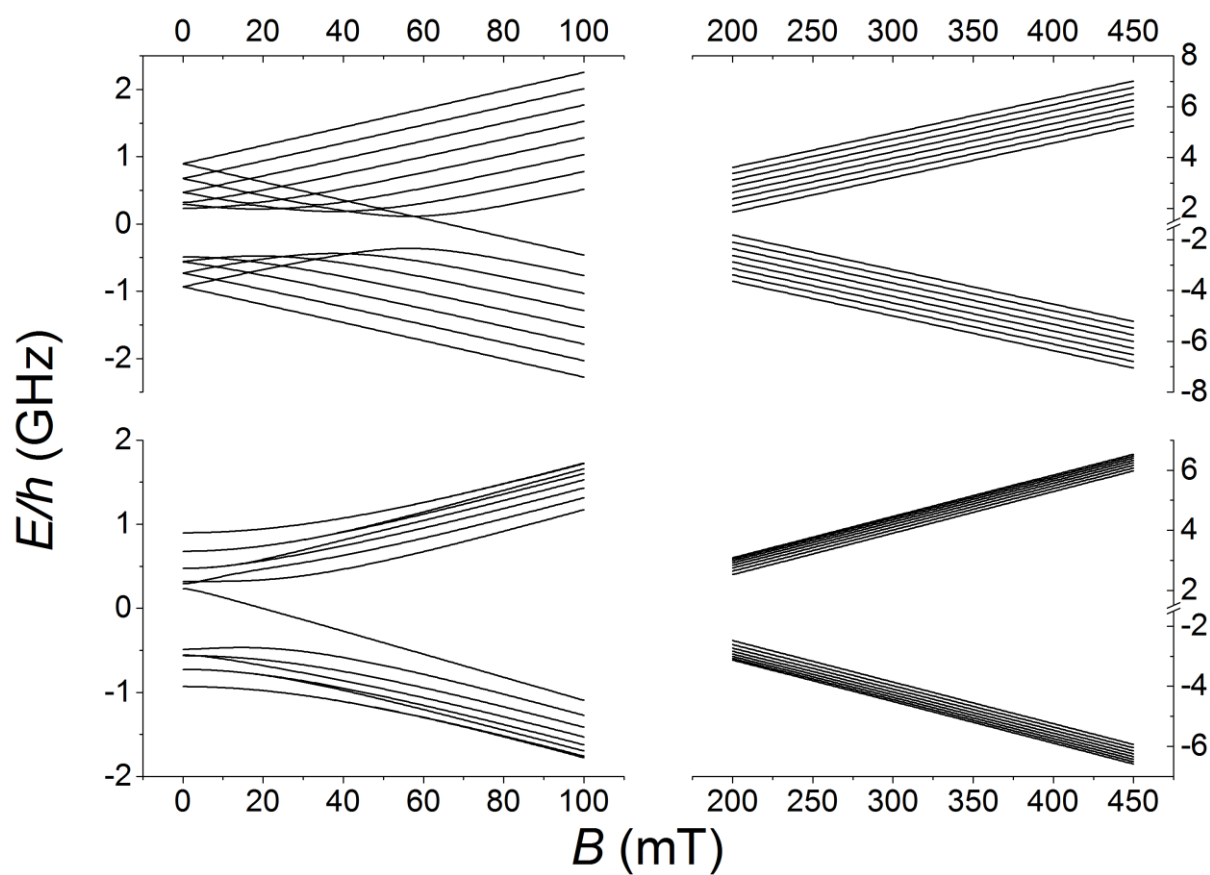


Figure S5. Energy levels diagrams of **1**, **2** and **3** when a magnetic field is applied along the largest hyperfine interaction component (upper) and along the smallest (lower). The diagrams were obtained with EASYSPIN on the basis of the Hamiltonian parameters extrapolated by the EPR simulations (Table S1).

3. X-Ray Microtomography

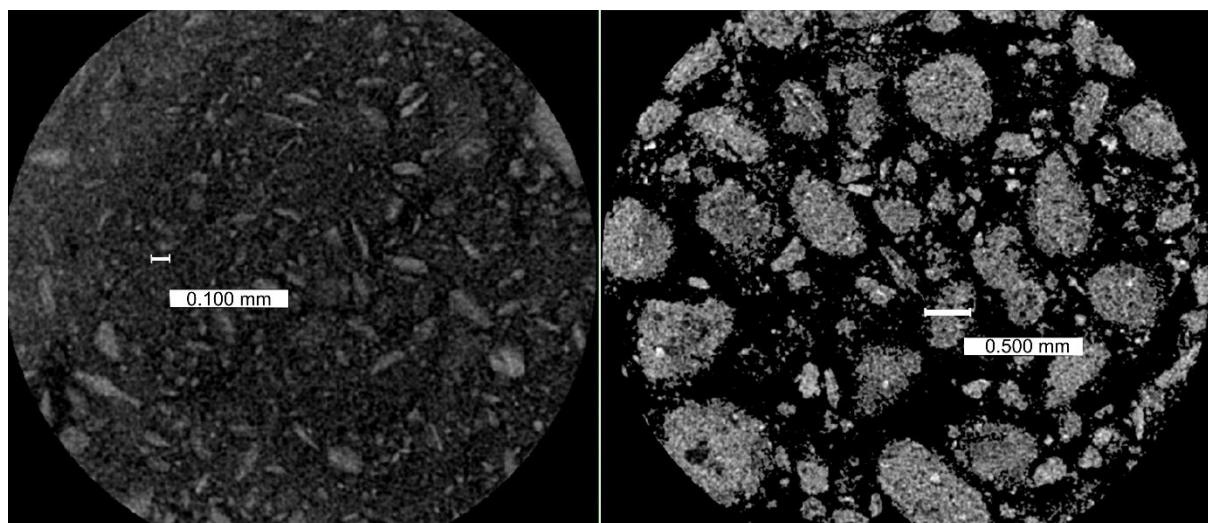


Figure S6. X-ray microtomography images of the finely crushed and pressed microcrystalline powder (left) and the moderately crushed crystals (right). White bars correspond to the indicated scale.

4. AC Susceptometry and Magnetometry

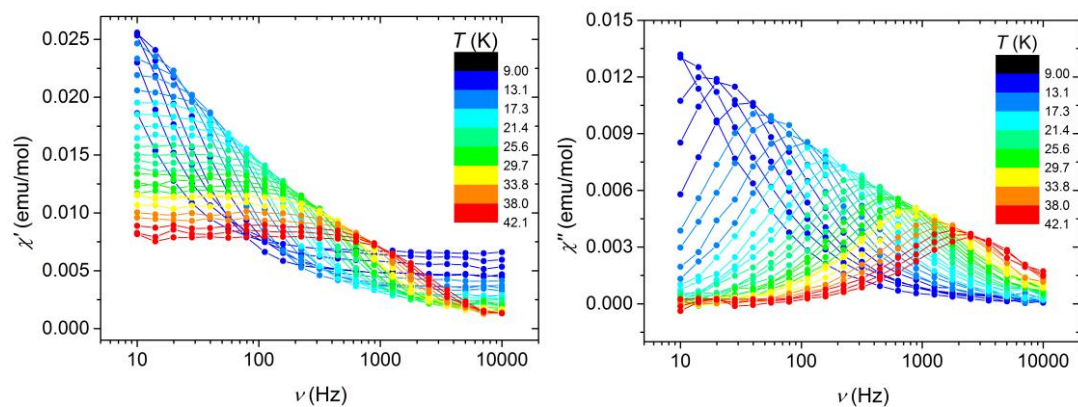


Figure S7. Frequency dependence of the real component χ' (left) and the imaginary component χ'' (right) of the magnetic susceptibility of **1a** as a function of the temperature (9.0–42 K range) under a static magnetic field of 0.2 T.

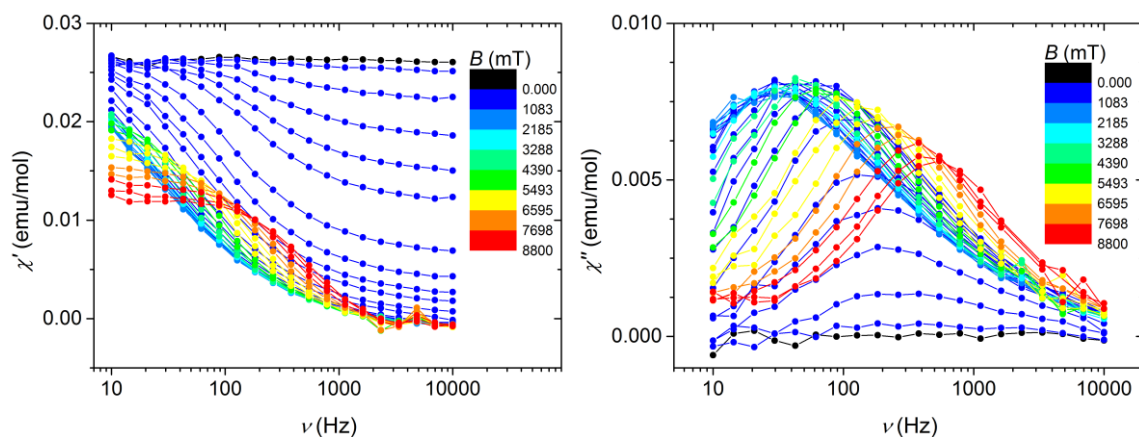


Figure S8. Frequency dependence of the real component χ' (left) and the imaginary component χ'' (right) of the magnetic susceptibility of **1b** as a function of the magnetic field (0.0–8800 mT range) at $T = 10$ K.

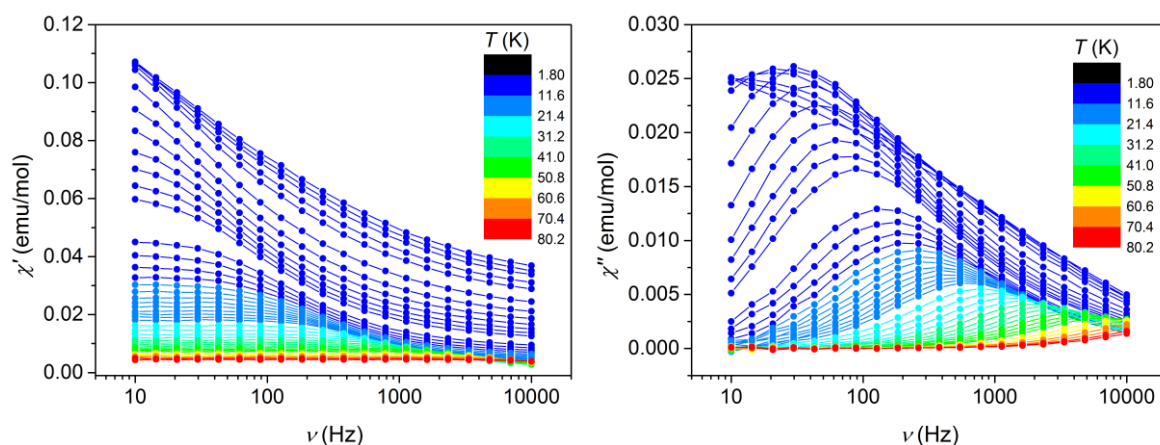


Figure S9. Frequency dependence of the real component χ' (left) and the imaginary component χ'' (right) of the magnetic susceptibility of **1c** as a function of the temperature (1.8–80 K range) under a static magnetic field of 0.2 T.

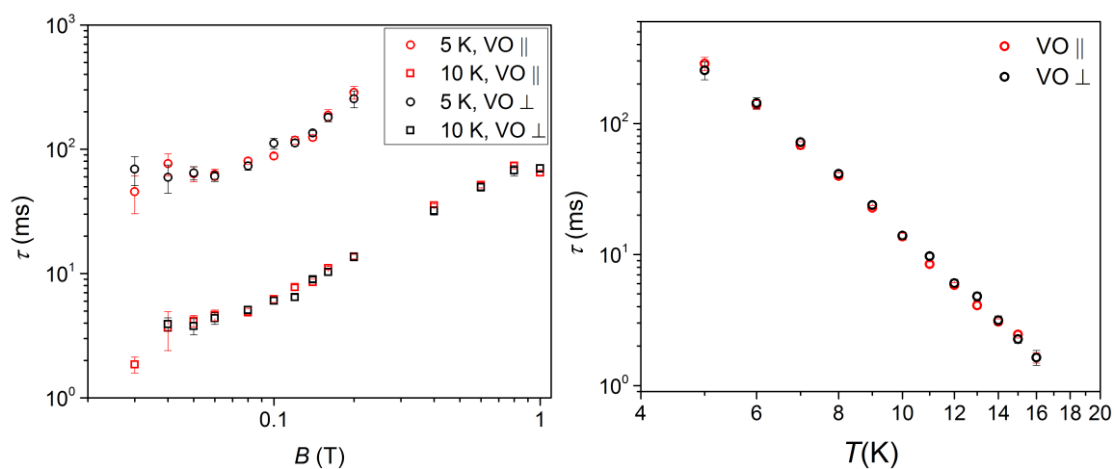


Figure S10. Spin-lattice relaxation time for a single crystal of **1** as a function of the static magnetic field at $T = 5$ and 10 K (left) and as a function of the temperature at $B = 0.2$ T (right) for both orientations between the static magnetic field and the vanadyl moiety.

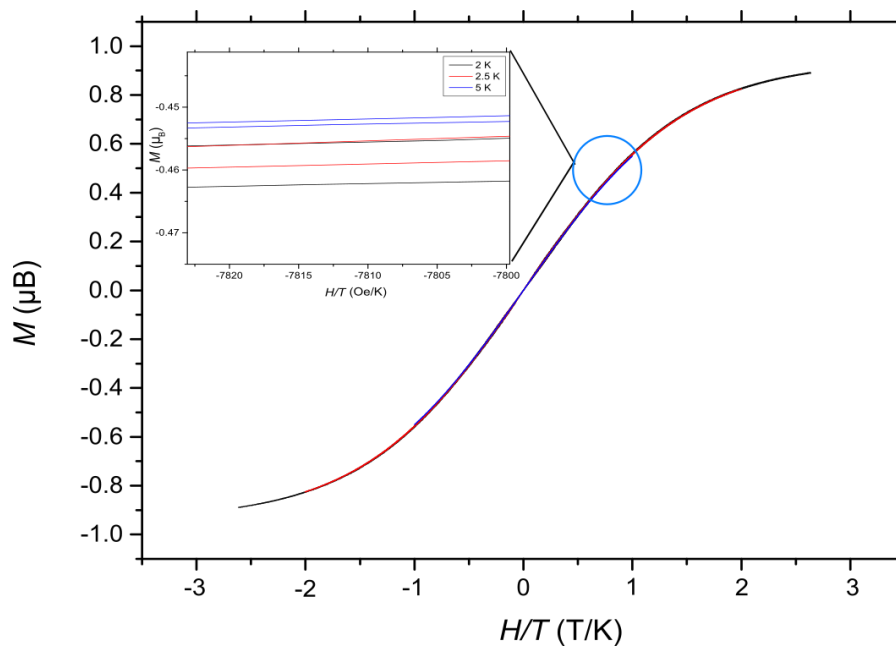


Figure S11. Magnetic hysteresis loops for **1a** at $T = 2, 2.5$ and 5 K with a field scan rate of 5 mT/s. The hysteresis opening at different temperatures is appreciable in the reported zoom.

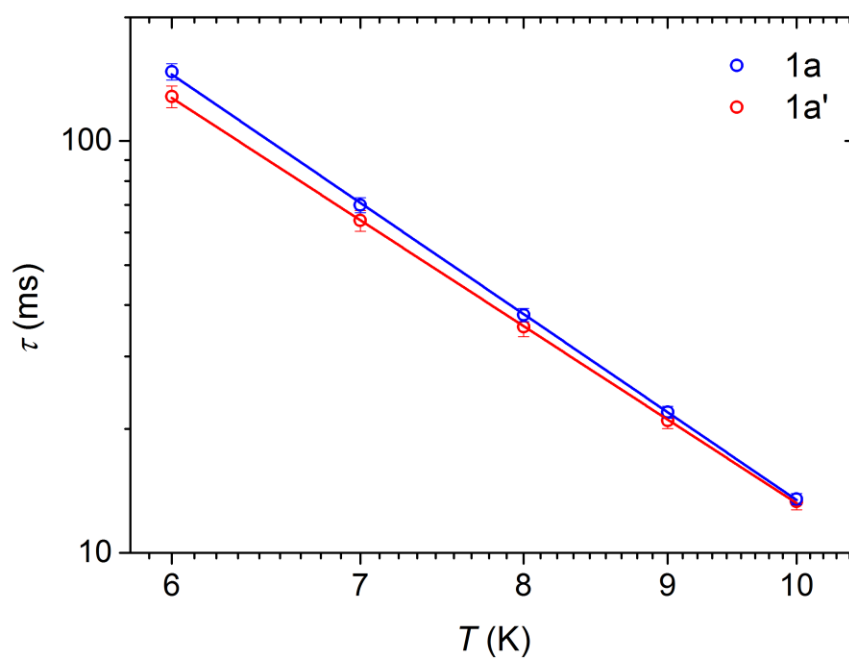


Figure S12. Temperature dependence (6–10 K range) of the spin-lattice relaxation time for **1a** and **1a'** under a static magnetic field of 0.2 T.

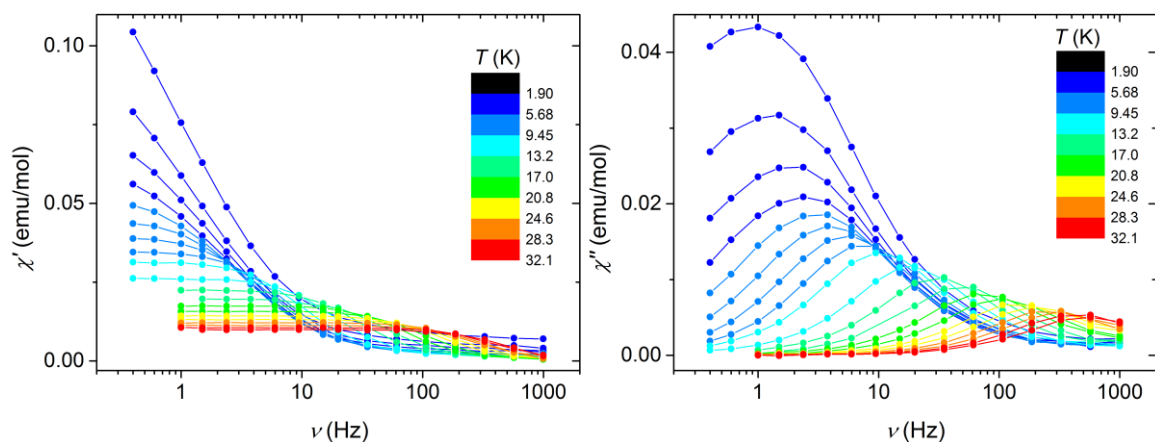


Figure S13. Frequency dependence of the real component χ' (left) and the imaginary component χ'' (right) of the magnetic susceptibility of **2a** as a function of the temperature (1.9–32 K range) under a static magnetic field of 0.2 T.

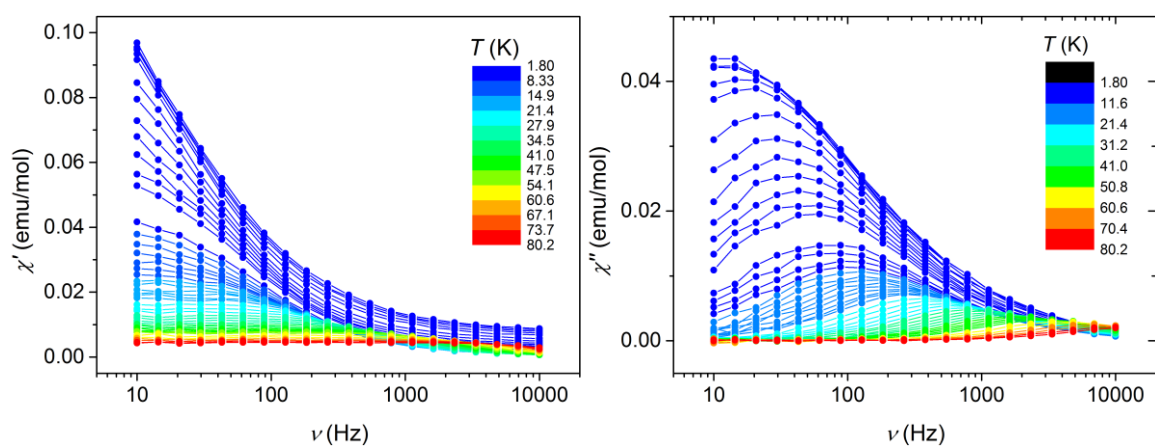


Figure S14. Frequency dependence of the real component χ' (left) and the imaginary component χ'' (right) of the magnetic susceptibility of **2c** as a function of the temperature (1.8–80 K range) under a static magnetic field of 0.2 T.

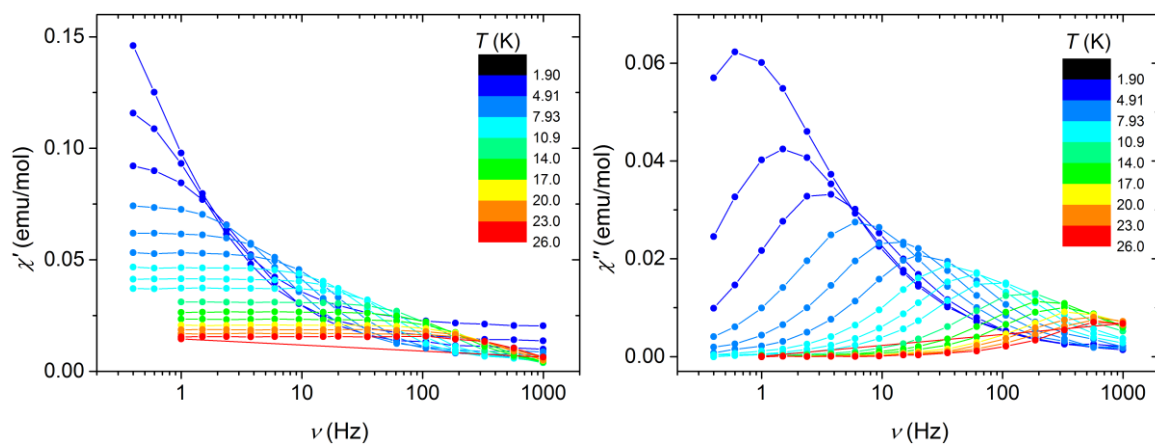


Figure S15. Frequency dependence of the real component χ' (left) and the imaginary component χ'' (right) of the magnetic susceptibility of **3a** as a function of the temperature (1.9–26 K range) under a static magnetic field of 0.2 T.

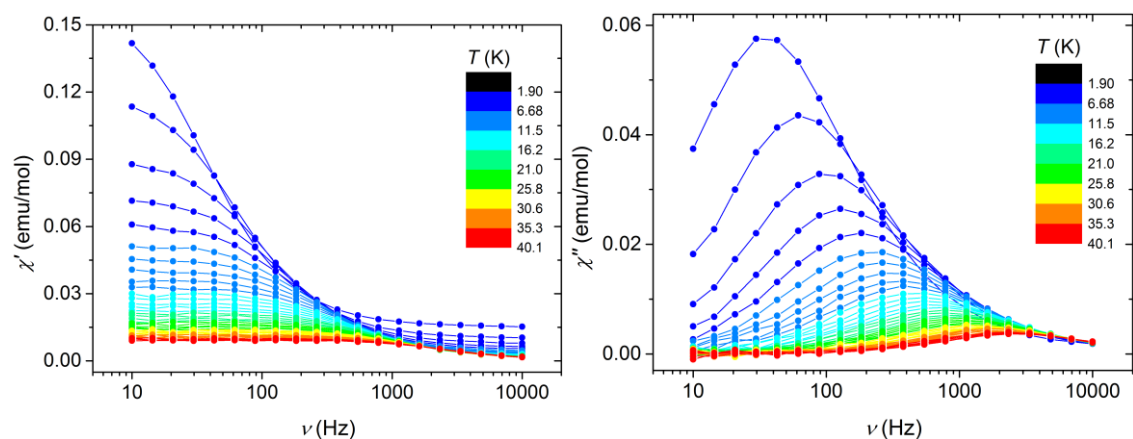


Figure S16. Frequency dependence of the real component χ' (left) and the imaginary component χ'' (right) of the magnetic susceptibility of **3c** as a function of the temperature (1.9–40 K range) under a static magnetic field of 0.2 T.

5. Force Field Calculations Validation

In Table S2 are reported the atoms position root mean square displacements (RMSD) for the FF and DFT optimized molecules of **1**, **2** and **3**, calculated against the experimental ones as reference. The latter have been extracted without modifications from their native crystalline environment.

Table S2. The reported values of nuclear RMSD are referred to the X-Ray structure and calculated on the whole molecule, hydrogen atoms included.

RMSD (Å)	1	2	3
FF	0.193	0.368	0.300
DFT	0.098	0.001	0.280

In Table S3, Table S4 and Table S5 are reported the primitive cell dimensions for **1**, **2** and **3**, optimized at both FF and pDFT levels, as described in the main text computational methods section.

Table S3. Unit cell parameters for **1** at both FF and pDFT level of modeling. For every entry, in parenthesis, the % error with respect to the X-Ray reference value is reported.

1	a (Å)	b (Å)	c (Å)	α (°)	β (°)	γ (°)
FF	7.213 (-1.8%)	7.6618 (-6.0%)	10.6967 (-4.6%)	81.50 (11.9%)	69.55 (-3.6%)	64.99 (-2.9%)
pDFT	7.487 (1.9%)	7.728 (-5.2%)	10.943 (-2.3%)	72.16 (-0.9%)	72.27 (0.1%)	65.68 (1.5%)
X-Ray	7.346	8.149	11.207	72.86	72.20	66.94

Table S4. Unit cell parameters for **2** at both FF and pDFT level of modeling. For every entry, in parenthesis, the % error with respect to the X-Ray reference value is reported.

2	a (Å)	b (Å)	c (Å)	α (°)	β (°)	γ (°)
FF	7.967 (-17.4%)	10.560 (5.3%)	12.300 (4.0%)	89.59 (-0.5%)	111.95 (2.9%)	91.26 (1.4%)
pDFT	9.077 (-5.9%)	10.477 (4.4%)	12.590 (-1.8%)	90.00 (0.0%)	108.10 (0.7%)	90.00 (0.0%)
X-Ray	9.649	10.032	12.819	90.00	108.84	90.00

Table S5. Unit cell parameters for **3** at both FF and pDFT level of modeling. For every entry, in parenthesis, the % error with respect to the X-Ray reference value is reported.

3	a (Å)	b (Å)	c (Å)	α (°)	β (°)	γ (°)
FF	15.309 (-7.0%)	19.617 (-3.2%)	15.066 (0.8%)	90.00 (0.0%)	89.89 (-0.1%)	90.00 (0.0%)
pDFT	16.320 (-0.8%)	19.786 (-2.4%)	14.344 (-4.0%)	90.00 (0.0%)	90.00 (0.0%)	90.00 (0.0%)
X-Ray	16.462	20.269	14.950	90.00	90.00	90.00

Although the quality of the DFT predicted structures is higher than the FF ones, the error introduced by lowering the level of theory is modest and the internal degrees of freedom, related to the first coordination shell, are reproduced within a few percentage points.

pDFT reproduces the unit cell parameters with a maximum absolute percent deviation

(MAPD) of 5.9% and a mean absolute percent error (MAPE) of 1.8%, while the FF calculations report a MAPD and a MAPE of 17.4% and 4%, respectively. Overall, the FF performs nicely and it increases the MAPE of only the 2% with respect to the excellent results obtained with pDFT.

However, significant deviations of a few parameters are observed when the FF is employed, pointing out that these kind of protocols and level of theory would always need a careful benchmark before production runs.

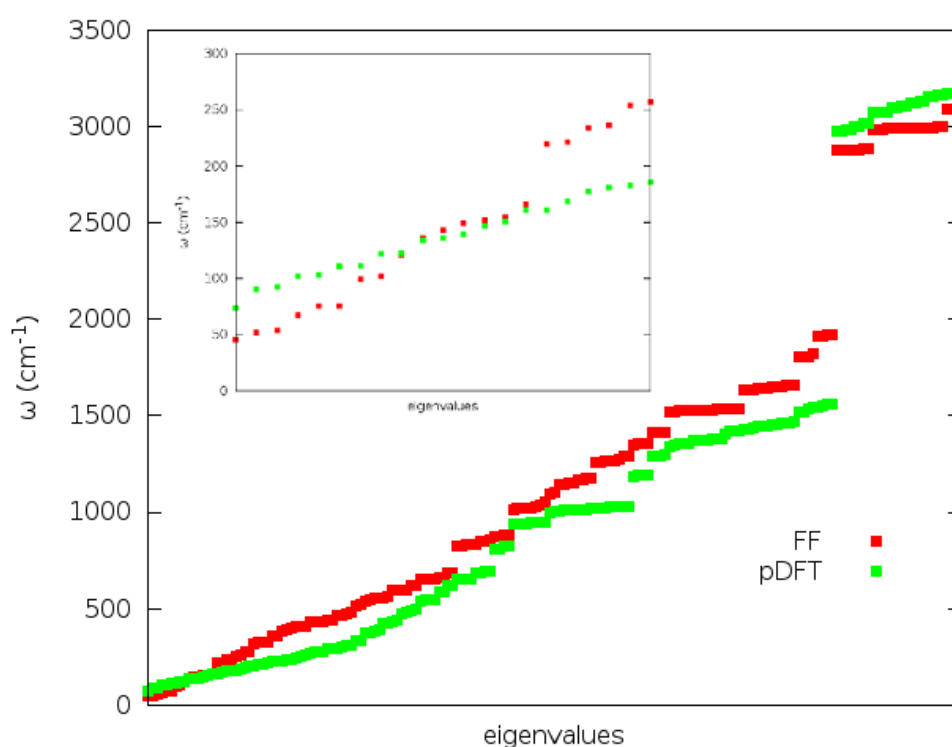


Figure S17. Dynamical matrix eigenvalues at the Γ point for the unit cell of **1**. The inset shows the low-energy region zoom.

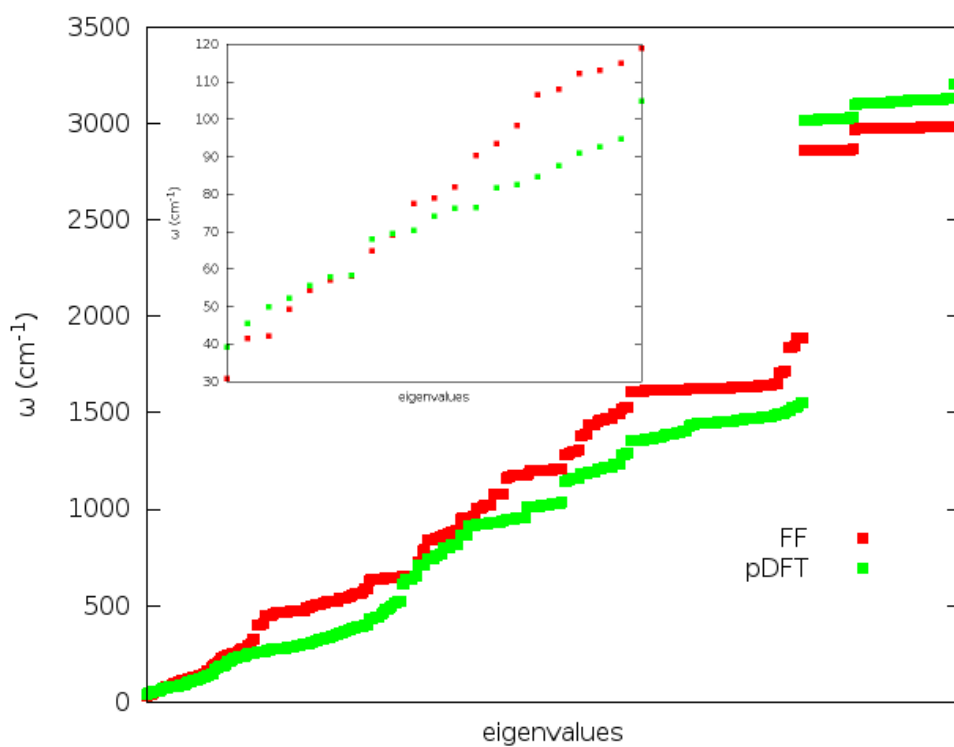


Figure S18: Dynamical matrix eigenvalues at the Γ point for the unit cell of **2**. The inset shows the low-energy region zoom.

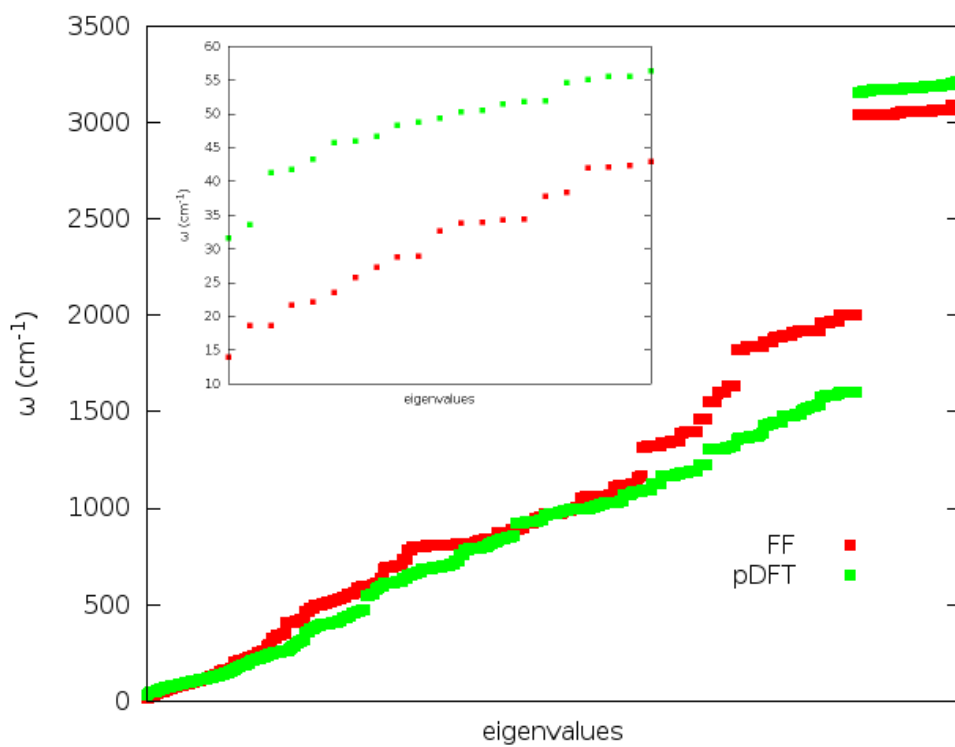


Figure S19: Dynamical matrix eigenvalues at the Γ point for the unit cell of **3**. The inset shows the low-energy region zoom.

For what concerns the vibrational frequencies, the degree of agreement between the experimental values and the computed one or between computational methods themselves rarely reach a high degree of accuracy, above all when only harmonic contributions are considered. This is to say that differences higher than 10% are not unlikely occurring even when comparing different ab initio methods^{S1} and also those FF trained to reproduce vibrational eigenvalues often show discrepancies from tens to hundreds cm^{-1} with respect to the training set.^{S2}

The degree of agreement between the vibrational frequencies computed at pDFT and FF level is reported in Figures S17 – S19. The obtained agreement is mainly qualitative but, and it is important to stress it, it is enough for the kind of comparative analysis we want to perform. Indeed, as shown by the insets, the trend in the low-energy part of the spectra for **1**, **2** and **3** is well reproduced: both FF and pDFT predict **1** to possess the higher low-lying frequencies and **3** to show the lower low-lying frequencies.

For these reasons we can safely consider the presented FF reliable enough for what concerns the considerations contained in the main article text.

5. References

S1 F. Neese, *Coord. Chem. Rev.*, 2009, **253**, 526-563.

S2 S. Grimme, *J. Chem. Theory Comput.*, 2014, **10**, 4497-4514.